Materials Horizons

ROYAL SOCIETY OF CHEMISTRY

COMMUNICATION

View Article Online
View Journal | View Issue

Cite this: *Mater. Horiz.*, 2024, 11, 6158

Received 1st August 2024,
Accepted 24th September 2024

DOI: 10.1039/d4mh01016g

rsc.li/materials-horizons

The role of temperature in the photoluminescence quantum yield (PLQY) of Ag_2S-based nanocrystals†

Peijiang Wang, [a] Rafael Morales-Márquez, [a] Gabriel Cervás, [b] Alejandro Hernández Medel, [cd] Marina Paris Ogayar, [d] D. Jimenez de Aberasturi, [efg] Ana Ines de Isidro-Gomez, [c] Almudena Torres-Pardo, [hi] Francisco Javier Palomares, [a] Saül Garcia-Orrit, [j] Célia T. Sousa, [c] Ana Espinosa, [a] Helmut H. Telle, [b] Dirk H. Ortgies, [dklm] Víctor Vega-Mayoral, [j] Juan Cabanillas-González, [j] Emma Martín Rodríguez, *[cdklm] Ute Resch-Genger, *[n] K. David Wegner *[n] and Beatriz H. Juárez *[a]

Highly emissive Ag_2S nanocrystals (NCs) passivated with a gradated shell incorporating Se and Zn were synthesized in air, and the temperature dependence of their photoluminescence quantum yield (PLQY) was quantified in both organic and aqueous media at ~1200 nm. The relevance of this parameter, measured at physiological temperatures, is highlighted for applications that rely on the near infrared (NIR) photoluminescence of NCs, such as deep NIR imaging or luminescence nanothermometry. Hyperspectral NIR imaging shows that Ag_2S-based NCs with a PLQY in organic media of about 10% are inefficient for imaging at 40 °C through 20 mm thick tissue with low laser irradiation power densities. In contrast, water-transferred Ag_2S-based NCs with an initial PLQY of 2% in water exhibit improved robustness against temperature changes, enabling improved imaging performance.

New concepts

This work presents a comprehensive study on the synthesis, structural analysis, and photophysical characterization of bright hydrophobic and hydrophilic Ag_2S-based nanocrystals (NCs). The NCs are synthesized *via* hot-injection of Ag_2S cores followed by selenium and zinc treatments. The Zn treatment conducted in air results in NCs with a higher photoluminescence quantum yield (PLQY), in comparison to those synthesized under nitrogen, a difference attributed to the different zinc content integrated into the NC lattice. For the first time, here we report on the temperature dependence of the PLQY of these NCs, both in organic and aqueous media. Hyperspectral NIR imaging under 20 mm tissue thickness underscores the importance of reporting PLQY variations with temperature, to establish a benchmark for the synthesis and evaluation of NCs for subcutaneous NIR imaging and luminescence nanothermometry.

Introduction

There is an increasing need for luminophores that emit in the second near-infrared transparency window (NIR-II, with wavelengths ranging from 1.0 μm to 1.7 μm) in various fields such as telecommunication, security systems, photovoltaics, and biomedical applications.[1–4] To push achievable sensitivities to the limit, many research activities are dedicated to strategies to improve the brightness of NIR-luminescent reporters and probes,

[a] *Materials Science Institute of Madrid, ICMM, Spanish Research Council, CSIC, C/Sor Juana Inés de la Cruz, 3, 28049 Madrid, Spain. E-mail: bh.juarez@csic.es*
[b] *Departamento de Química Física Aplicada, Facultad de Ciencias, Universidad Autónoma de Madrid, C/Francisco Tomás y Valiente 7, Madrid, 28049, Spain*
[c] *Departamento de Física Aplicada, Facultad de Ciencias, Universidad Autónoma de Madrid, C/Francisco Tomás y Valiente 7, Madrid, 28049, Spain*
[d] *Nanomaterials for BioImaging Group (NanoBIG), Facultad de Ciencias, Universidad Autónoma de Madrid, C/Francisco Tomás y Valiente 7, Madrid, 28049, Spain*
[e] *SpainCiCbiomaGUNE, Basque Research and Technology Alliance (BRTA), Miramon Pasealekua, 182, 20014 Donostia-San Sebastián, Gipuzkoa, Spain*
[f] *Centro de Investigación Biomédica en Red de Bioingeniería, Biomateriales and Nanomedicina (CIBER-BBN), 20014 Donostia-San Sebastián, Spain*
[g] *Ikerbasque, Basque Foundation for Science, 48009 Bilbao, Spain*
[h] *Inorganic Chemistry Department, Chemical Sciences Faculty, Universidad Complutense de Madrid, 28040 Madrid, Spain*
[i] *ICTS National Center for Electronic Microscopy, Universidad Complutense, 28040 Madrid, Spain*
[j] *IMDEA Nanoscience, Faraday 9, Campus de Cantoblanco, 28049 Madrid, Spain*
[k] *Nanomaterials for BioImaging Group (nanoBIG), Instituto Ramón y Cajal de Investigación Sanitaria (IRYCIS), Ctra. Colmenar Viejo, km. 9,100, 28034 Madrid, Spain. E-mail: emma.martin@uam.es*
[l] *Institute for Advanced Research in Chemical Sciences (IAdChem), Universidad Autónoma de Madrid, 28049 Madrid, Spain*
[m] *Instituto de Ciencia de Materiales Nicolás Cabrera, Universidad Autónoma de Madrid, 28049 Madrid, Spain*
[n] *Bundesanstalt für Materialforschung und -prüfung (BAM), Richard-Willstaetter-Str. 11, 12489 Berlin, Germany. E-mail: karl-david.wegner@bam.de, ute.resch@bam.de*

† Electronic supplementary information (ESI) available: eSI-S1 – on procedural aspects; eSI-S2 – information related to experimental results. See DOI: **https://doi.org/10.1039/d4mh01016g**

i.e., the product of the photoluminescence quantum yield (PLQY) and the molar absorption coefficient or absorption cross section at the excitation wavelength. High brightness, which controls the size of the resulting luminescence signals from the material side, is crucial for both diagnostic and therapeutic approaches, including NIR imaging,[5–7] and luminescence nanothermometry (LNT).[8] LNT is a non-invasive technique used to measure temperature and temperature variations with nanometer resolution by exploiting the temperature-dependent photoluminescence (PL) of luminophores. Luminophores commonly employed for LNT are colloidal semiconductor nanocrystals (NCs), including quantum dots (QDs), rare-earth-doped nanoparticles, organic dyes, and fluorescent proteins.[9] LNT has been employed to measure the temperature within living cells[10] or in organs such as the brain[11] or the liver in *in vivo* mice models.[12] A common requirement for all NIR imaging and LNT probes is a sufficiently high efficiency of light emission, which is determined by the PLQY. PLQY is defined as the ratio of the number of emitted photons to that of absorbed photons. In addition, a high absorption cross section at the chosen excitation wavelength is advantageous. The figure of merit in LNT is the relative thermal sensitivity (S), defined as the temperature dependence of the rate of change of a particular PL indicator (*e.g*, intensity, PL intensity ratio, peak position, lifetime, *etc.*)[8,13–15] Alternatively, temperature coefficients can be utilized for LNT comparison as done, *e.g.*, for lanthanide-based systems, which enable ratiometric measurements.[16]

For NCs or other luminophores, in which the temperature dependence of the PL is exploited for local temperature monitoring, the PLQY is commonly measured at room temperature (RT). However, to fully characterize these systems and better evaluate their performance as luminescent nanothermometers, PLQY values at physiological body temperatures and/or the temperature dependence of their PLQY should be provided. Likewise, for *in vivo* PL imaging, in addition to the essential low cytotoxicity of the respective reporters, knowledge of the temperature dependence of their PLQY at physiological body temperatures is crucial, as such experiments are performed at relatively elevated temperatures compared to typical spectroscopic studies performed at RT. However, the temperature dependence of PLQY is scarcely reported for many luminophores. The temperature-dependent PLQY values can also provide detailed information on the PL mechanisms, which complement the simpler relative changes covered by thermal sensitivity values. Together, these measurements offer an improved and more comprehensive understanding of the thermal behavior of luminophores.

A promising NIR imaging and LNT probe is nanocrystalline silver sulfide (Ag_2S), with its PL band centered at approximately 1200 nm for the bulk material. These NCs reveal a low cytotoxicity when covered with a robust biocompatible shell.[17] Because of its small band gap of about 1.1 eV, Ag_2S has also found applications in photovoltaics, particularly as a sensitizer in solar cells.[18] As narrow band gap semiconductor, Ag_2S is highly prone to quenching due to thermal excitations and non-radiative recombination, which strongly restricts its PLQY at RT and above. The bohr radius of Ag_2S is approximately 2.2 nm,[19] which limits the observation of quantum confinement effects to very small NCs. Ag_2S NCs can be synthesized in both aqueous and organic solvents where synthetic recipes are mainly carried out under N_2.[14] The latter is the preferred route for obtaining NCs with improved crystallinity and PL response. In organic solvents, Ag_2S NCs can be prepared by the thermal decomposition (commonly known as heat-up) of a silver salt [usually silver(I) diethyldithiocarbamate, (AgDDTC)] in dodecanethiol (DDT) at approximately 200 °C.[20] This strategy yields micrometer-sized superlattices of NCs with sizes of about 5 nm and a PLQY of 2.5% at RT in tetrachloroethene (TCE).[21,22] The formation of these superlattices is the result of the formation of silver(I) dodecanethiolate, an intermediate lamellar product formed during the decomposition reaction, where the NCs nucleate and grow.[21,22] NCs obtained from metal thiolates have been previously reported for other systems such as $Cu_{2-x}S$ and $CuInS_2$.[23,24]

Sonication in chloroform can be used to untangle the NC superlattices and obtain individual NCs.[25] Alternatively, the reaction can be performed in toluene. This strategy, that prevents the formation of the lamellar-like intermediate, allows to obtain individual NCs by hot injection of a sulphur source.[21] The treatment of these Ag_2S NCs with a selenium solution, Se@TOP, leads to core/shell $Ag_2S/Ag_2(S,Se)$ structures with improved PLQY with respect to the Ag_2S NCs cores, although typical PLQY values are still below 1%.[21]

A straightforward and common methodology to increase the PLQY of NCs, particularly QDs, is the passivation of the NC surface with a higher-bandgap semiconductor. This strategy was exploited to passivate Ag_2S with a ZnS shell in droplet microreactors,[26] through microwave assisted reactions,[27–29] or by wet chemistry procedures,[30,31] including hydrothermal approaches.[32,33] Other alternatives to enhance the PL properties of Ag_2S NCs involve the use of femtosecond laser pulses on Ag_2S NCs in chlorinated solutions, yielding PLQY values of approximately 10% at RT.[34] Similarly, the sonication of Ag_2S NCs in chloroform can also increase the PLQY up to values of 10% at RT due to surface etching.[35,36]

In this study, an alternative and straightforward approach for fabricating Ag_2S NCs with improved PL properties is reported, relying on the hot-injection synthesis of Ag_2S followed by Se and Zn treatments, in air. This strategy yields NCs with PLQY values of $\sim$10% at RT in TCE. As evidenced by X-ray photoelectron spectroscopy (XPS), Zn diffuses through the $Ag_2S/Ag_2(S,Se)$ core/shell structure, producing NCs with a mixed shell that includes ZnS. In contrast to other studies,[30,31] the ZnS shell forms without addition of a sulphur precursor, but as reported previously[30] it can be considered a cation exchange process. The subsequent characterization of these bright NCs as dual NIR emitting reporters and luminescent nanothermometers for biological media was enabled by encapsulation by a well-known biocompatible amphiphilic polymer, utilized previously to stabilize nanothermometers in water.[37,38] In this work, the temperature dependence of the PLQY of our Ag_2S-based NCs was determined in the physiologically relevant temperature range in organic and aqueous media. The impact of PLQY values on temperature was assessed in sub-tissue imaging experiments

using hyperspectral NIR imaging at approximately 40 °C, with low excitation power densities ranging from 0.4 to 50 mW cm^{-2} and fast acquisition times of up to 100 ms. The temperature-dependent PLQY data of Ag_2S-based NCs obtained in this study can be used as a solid basis for comparing different Ag_2S-based NCs and predicting their performance in bioimaging studies and LNT under biologically relevant conditions.

Results and discussion

The synthesis route used to produce bright Ag_2S NCs is shown in Fig. 1a. Briefly, after synthesizing Ag_2S NCs cores (C-cores hereafter) from AgDDTC and DDT in toluene, the resulting NCs were treated with Se@TOP, leading to a shell in which Ag atoms are bound to S and Se, thus forming an $Ag_2S/Ag_2(S,Se)$ core/shell structure (CS hereafter) according to previously performed X-ray absorption spectroscopy (XAS).[21] In the second step, these NCs were treated with a zinc oleate ($Zn(OA)_2$) solution to passivate the NC surface and improve the optical properties by growing a Zn chalcogenide shell (NCs named CSS hereafter). This route was explored under different conditions, *i.e.*, under N_2 atmosphere and in the presence of air, and will be further discussed (see also eSI-S1, eS-S2, ESI†). Furthermore, to preserve the optical properties of the CSS NCs, their encapsulation using the amphiphilic ligand dodecylamine-modified polyisobutylene-*alt*-maleic anhydride (N-PMA),[25] has been performed. N-PMA has been used before for the bio-compatibilization of metallic, oxide, and semiconductor NPs,[39–42] and has also been employed to render Ag_2S NCs produced by a heat-up synthesis biocompatible.[25]

Fig. 1b shows a series of optical images of the silver precursor solution taken at different reaction times, where the color of the solution changes from yellow to orange and to dark red. As observed in Fig. 1c, the PL spectra of these solutions reveals a PL band spanning the range 350 to 600 nm, which does not vary with time (no PL was detected in the NIR range). This indicates that the observed colors during this step are not the result of quantum-confined NCs growing in the solution. The color variations are tentatively attributed to the evolution of the previously mentioned silver(I) dodecanethiolate lamellar product.[43]

To enable the controlled growth of individual Ag_2S NCs at low reaction temperatures, in our case 100 °C, the injection of a sulphur stock solution in the previously mentioned silver precursor is required. We found that the timing of this injection influenced the overall PL intensity of the final Ag_2S NCs, as shown in Fig. S1 in eSI-S2 (ESI†). The highest PL intensity was observed when the injection was performed during the late stage of AgDDTC decomposition, *i.e.*, when the colour of the precursor solution shifts from orange to red. NC size analysis by HRTEM revealed a slight increase in size from ~7.4 nm to ~8.4 nm, depending on the injection time.

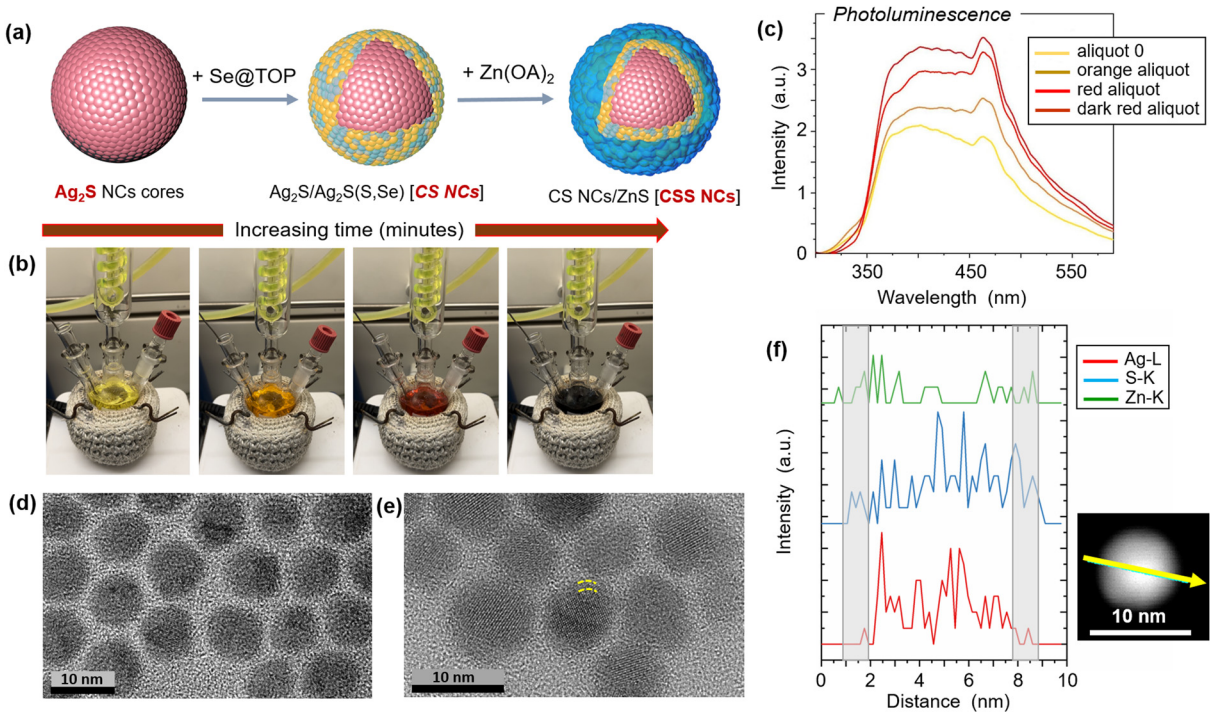

Fig. 1 (a) Schematic presentation of Ag_2S cores treated with Se (CS) and Zn precursors, to obtain a better-passivated surface in the final CSS structures. (b) Optical images showing the evolution of the silver precursor solution, at temperatures of 100–110 °C. (c) Emission spectra of the precursor solutions, associated with the colors apparent in (b), *i.e.*, yellow, orange, red, and dark-red, respectively. (d) and (e) HRTEM images of CS and CSS NCs, respectively; in (e) a more crystalline core, surrounded by a more amorphous phase, indicated by the yellow dash lines, is apparent. (f) EDX line profiles, evidencing a predominant presence of Zn on the outer part of the NCs, along with a simultaneous decrease in Ag content (shadow areas), pointing out to the formation of ZnS shell.

The largest size was observed for the late-stage injection (see Fig. S1 in eSI-S2, ESI†). Although the average sizes are similar and experimental variations in the synthesis can influence these values, we believe that the evolution of the silver(I) dodecanethiolate lamellar intermediate product plays a crucial role. Further studies, which are beyond the scope of this paper, are needed to clarify the molecular structure of the intermediate over time and its correlation with the final average size of the NCs obtained. The PL emission maxima of all Ag_2S NPs cores were located at approximately 1200 nm, which corresponds to the emission of bulk Ag_2S. Thus, we ascribe the higher PL intensity observed for larger NCs to their stronger absorption. Additional details of sample synthesis and measurement procedures are provided in the ESI,† eSI-S1.

Fig. 1d and e show the HR-TEM images of the CS and CSS NCs, respectively. In all cases, highly crystalline NCs were obtained. The average size of CS NCs is approximately 8.0 ± 0.6 nm (Fig. 1d). A similar size distribution was observed for the pure Ag_2S NC cores. However, for the Zn-treated samples (such as those shown in Fig. 1e), a slight increase in size distribution by (about 1.0 nm was observed), but the average size was maintained. As shown in Fig. 1e, the Zn treatment also leads to a slight modification of the initial morphology, *i.e.*, yielding more polyhedral NCs. Additionally, a shell marked with two dashed lines can be inferred (see also Fig. S2 in eSI-S2, ESI†). This scenario fits well with Zn atomic diffusion and/or cation exchange, a strategy amply used to controllably manipulate the optical properties and PLQY of several types of NCs.[30,44,45]

Fig. 1f shows the analysis of the EDS spectrum, which has been acquired across the CSS NC marked with an arrow (in the inset). The corresponding X-ray intensity profile confirms the presence of NCs with a composition close to that of stoichiometric Ag_2S and the presence of a ZnS rich shell, which should probably be the result of Zn diffusion along the initial crystalline CS lattice. The low concentration of Se limits its detection during the spectrum acquisition, which was done within a few seconds, to preserve the integrity of the NC. However, evidence of the presence of Se was clearly visible at longer exposure times (see Fig. S2 in eSI-S2, ESI†) and by inductively coupled plasma (ICP) spectroscopy analysis where 2.5 at% of Se is detected (eSI-S1, ESI†). However, long exposure times under an electron beam can affect the morphology/distribution of the elements composing the NC shell, and therefore can limit the spatial resolution for the determination of elements at sub-nanometer resolution.

The spectroscopic properties of the resulting NCs are shown in Fig. 2; note that all synthesis steps were performed in air (details in eSI-S1, ESI†). Fig. 2a shows the extinction spectra of the Ag_2S NC cores, CS NCs, and CSS NCs. The spectra of the NCs before and after Se@TOP and $Zn(OA)_2$ treatments showed similar properties, with a featureless absorption tail; this is expected in the absence of quantum confinement effects. The different samples revealed small differences in the optical density values above 400 nm. In the case of the CS samples, the slight increase in scattering after Se treatment might be due to a slightly higher aggregation tendency of CS NCs compared

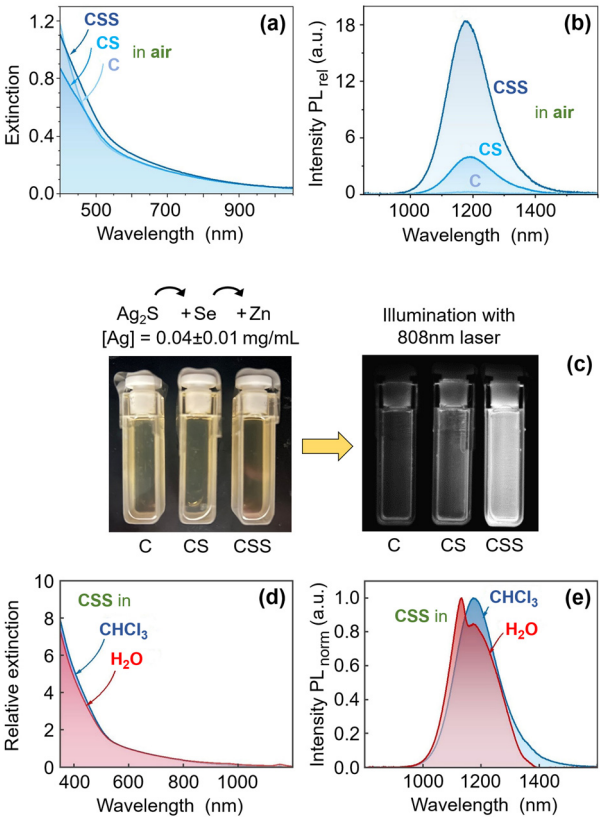

Fig. 2 (a) Extinction and (b) PL spectra of Ag_2S NCs cores, CS and CSS NCs, in air. (c) Optical images of the Ag_2S NCs cores, CS and CSS NCs solution samples without (left) and with (right) illumination with a NIR laser (808 nm). (d) Extinction and (e) PL responses of CSS NCs, dispersed in water and in chloroform.

to that of the Ag_2S NCs cores. For CSS NCs treated with $Zn(OA)_2$, the higher extinction at approximately 400 nm can be ascribed to the absorption of ZnS. Fig. 2b shows the corresponding PL spectra, exhibiting a very strong increase in PL intensity after Se treatment, and even more so after Zn treatment. An additional feature is a slight relative shift in peak position, which is evident when normalizing the PL spectra after the Se and Zn treatments (see Fig. S5 in eSI-S2, ESI†). These small shifts can be ascribed to minor differences in the formed band gap structure of the modified Ag_2S lattice after Se and Zn treatments.[26] Fig. 2c compares optical images of diluted solutions of the Ag_2S NC cores, CS, and CSS (Ag concentration, [Ag] = 0.04 ± 0.01 mg mL^{-1}) without (left images) and with illumination (right images) with light from an 808 nm laser, highlighting the PL enhancement. [Ag] corresponds to the atomic concentration of the three NCs solutions measured by ICP spectroscopy (see eSI-S1, ESI†).

The application of these NCs as NIR imaging probes and/or nanothermometers for biological studies requires water dispersible NCs. This was achieved by surface modification with the copolymer N-PMA. This biocompatible polymer intercalates between the alkyl chains of the initially present hydrophobic surface ligands of the NCs prepared in organic solvents. This approach has been recently used to passivate Ag_2S NCs,

produced by heat-up synthesis.[25] Fig. 2d shows the extinction spectra of the NC samples in chloroform ($CHCl_3$) and in water after treatment with N-PMA, confirming their close match and no increase in scattering due to aggregation. The shapes of the PL spectra (Fig. 2e) changed slightly after transfer to water, owing to the water absorption band at around 1200 nm.

As previously mentioned, the synthesis of Ag_2S NC cores, as well as CS and CSS NCs, was explored under varying conditions, specifically in N_2 and in air. Interestingly, we found that the formation of Ag_2S NC cores and CS NCs is minimally affected by the presence of oxygen. However, the treatment with the Zn precursor significantly influences the final PL response. Notably, the PL response is higher when the CSS samples are synthesized in air. To understand the origin of this effect, we have explored the surface chemistry of the CSS NCs produced in air and N_2 with XPS in combination with Ar–ion bombardment. This methodology allows the extraction of photoelectrons at different penetration depths from the particle (see Fig. S3 for further details, eSI-S2 ESI†). These studies confirm the presence of a gradient of the chemical composition from the outer shell surface, rich in ZnS, to regions closer to the inner core, rich in Ag_2S. The results also support the Zn diffusion and/or cation exchange hypothesis. Furthermore, the comparative studies shown in Fig. S3 and S4 (eSI-S2 ESI†) provide evidence for the higher integration of Zn in samples produced in air. The strategy to produce robust and efficient QDs emitters by alloying the structure from the core to the shell is well-known for several QD systems.[46,47]

Transient absorption spectroscopy (TAS) measurements

To provide further insights into the photophysics of Ag_2S NCs and the effect of Se and Zn passivation on the optical properties, transient absorption spectroscopy (TAS) measurements were performed with NCs dispersions pumped with different laser pulse energy densities (mJ cm^{-2}). Such studies are of particular interest because many-body effects, such as multi-exciton generation (MEG) or Auger recombination, have been reported in Ag_2S QDs.[48,49] Although we did not expect MEG in these samples, because of the small excess of energy of pump photons (used laser 775 nm, 1.6 eV) with respect to the bandgap of Ag_2S, the presence of other many-body processes cannot be excluded. Auger recombination was evaluated by performing a TAS study at different fluences, namely 0.16, 0.32, 0.6, and 1.29 mJ cm^{-2}. Note that these pump fluences are within the linear absorption range, as confirmed by the linear scaling of the TAS signal at 1033 nm (see Fig. S6 in eSI-S2, ESI†).

To elucidate the role of Se and Zn in the suppression of surface defects, which could contribute to the observed PL enhancement, the dynamics of the excited states of the Ag_2S cores and CSS NCs were investigated. The TAS contour plot of Ag_2S (Fig. 3a) shows broad photobleaching (PB), visible as a positive $\Delta T/T$ in the 950–1130 nm spectral region, accompanied by excited-state absorption ($\Delta T/T < 0$) above 1130 nm. These two main spectral features are in agreement with previous TAS measurements of Ag_2S NCs.[22,50] During the first 3 ps, the PB band shifts towards lower energies. This shift has been ascribed to different processes, such as thermalization of hot excitons[51] bandgap renormalization,[52] the Burstein–Moss effect,[53] or the Stark effect due to photoexcited charges.[54] After the initial evolution, the TAS signal undergoes a monotonic decay, typically assigned to band-to-band recombination. The contour plot for CSS NCs is shown in Fig. 3b. Fig. 3c and d depict the TAS spectra of the Ag_2S NCs cores and CSS NCs at

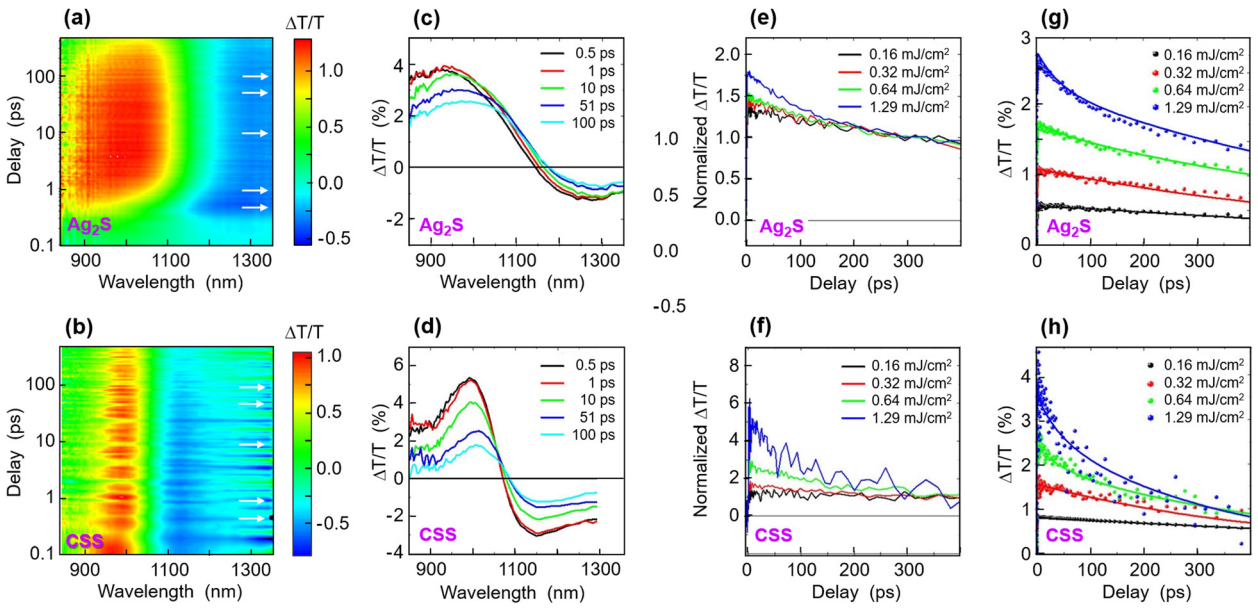

Fig. 3 Transient Absorpton Spectroscopy (TAS) contour plot of (a) Ag_2S and (b) CSS NCs pumped at 775 nm, with 0.16 mJ cm^{-2}. The arrows indicate the contour slices shown in (c) and (d). (c) and (d) TAS spectra pumped at 775 nm, with 0.16 mJ cm^{-2}, at different pump–probe delays of Ag_2S NCs cores and CSS, respectively. (e) and (f) TAS dynamics at 1033 nm, normalized at 300 ps, of Ag_2S NCs cores and CSS, respectively, pumped with different energy fluences: 0.16 (black), 0.32 (red), 0.6 (green) and 1.29 (navy) mJ cm^{-2}. (g) and (h) TAS dynamics at 1033 nm of Ag_2S NCs cores and CSS, respectively; the solid lines correspond to global fits.

different pump–probe delays, respectively. These spectra constitute slices through the contour plots in Fig. 3a and b, for the delays indicated by the white arrows. As it can see in Fig. 3d, Zn passivation has a strong impact on the TAS spectra, leading to narrower PB and excited state absorption (ESA) bands with steeper onsets. This is compatible with the reduction of the number of defects in CSS NCs with respect to the Ag_2S cores. The blue shift of the isosbestic point in CSS NCs suggests a slight reduction in core size.

These effects were accompanied by an overall faster decay of the TAS features, in comparison to the bare Ag_2S NCs cores. The TAS kinetics monitored close to the PB maximum (1033 nm) exhibited a stronger pump energy fluence dependence for the CSS than in the Ag_2S NCs cores (Fig. 3e and f). It is noteworthy that the TAS kinetics of CSS NCs reveal a larger pump fluence-dependence, confirming a more pronounced Auger recombination compared to Ag_2S NCs cores. We attribute this to a stronger carrier diffusion, owing to a lower concentration of trapping defects in the former. The TAS spectra and dynamics were fitted by combining singular value decomposition and global analysis, to reveal the different carrier relaxation processes and their corresponding timescales.

The good agreement between the fits and the experimental data is illustrated in Fig. 3g and h. Low fluence kinetics (0.16 and 0.32 mJ cm^{-2}) were successfully reproduced with a simple model involving two sequential processes, namely fast carrier thermalization (<1 ps) and band-to-band recombination ($\sim$100 ps). On the other hand, to model the TAS kinetics at 0.6 and 1.29 mJ cm^{-2} an intermediate Auger recombination process is needed in the relaxation sequence. The proposed model accurately reproduced all TAS measurements (see Fig. S7 and S8 in eSI-S2, ESI†). It is noteworthy that the obtained Auger recombination parameter is larger in CSS NCs (7×10^{-3} ps^{-1} cm^6) than in Ag_2S only cores (5.8×10^{-3} ps^{-1} cm^6), indicating that after surface passivation, processes competing with Auger recombination (such as charge carrier trapping in defects) diminish in importance.[55]

This indicates that the surface of CSS NCs is better passivated than that of Ag_2S NCs by the plausible formation of a shell. The larger carrier diffusion in CSS NCs is compatible with the observed longer PL lifetimes from the time-resolved PL measurements. As shown in Fig. S9 in eSI-S2 (ESI†), the PL decay dynamics exhibited a large increase in the average fluorescence lifetime from approximately 50 $\pm$ 4 ns for Ag_2S NCs cores to 360 $\pm$ 3 ns for CS and 817 $\pm$ 4 ns for CSS NCs.

Synchrotron X-ray absorption spectroscopy (XAS)

To gain an in-depth understanding of structure and chemical composition of the passivation shell as well as aging information (*i.e.*, modification of the chemical composition with time), we performed X-ray absorption spectroscopy (XAS) at the synchrotron ESRF (BM30 beamline, Grenoble, France), including X-ray absorption near-edge structure (XANES) and extended X-ray absorption fine structure (EXAFS). XANES provides information regarding the oxidation state, whereas EXAFS offers insights into the local environment around the absorbing Ag ions, including the atomic distances and coordination numbers of the surrounding shells.

The combination of these techniques allows for an in-depth structural analysis, detailing the Ag short-range geometry, and identifying the phases and their reduction–oxidation trends. Using these two techniques, we assessed and compared CS and CSS samples in $CHCl_3$ and water, for the latter surface-capped with N-PMA, 11 months after their synthesis (samples stored in air, within the fridge). Fig. 4a shows the XANES spectra at the Ag K-edge (25 514 eV) of the samples in $CHCl_3$ and in water, encapsulated in N-PMA (fluorescence mode).

In order to observe any sign of oxidation, the spectra of the samples were compared to those of Ag_2S and Ag_2O bulk standard materials. As seen in Fig. 4a, no apparent differences were observed between the different samples, pointing to a

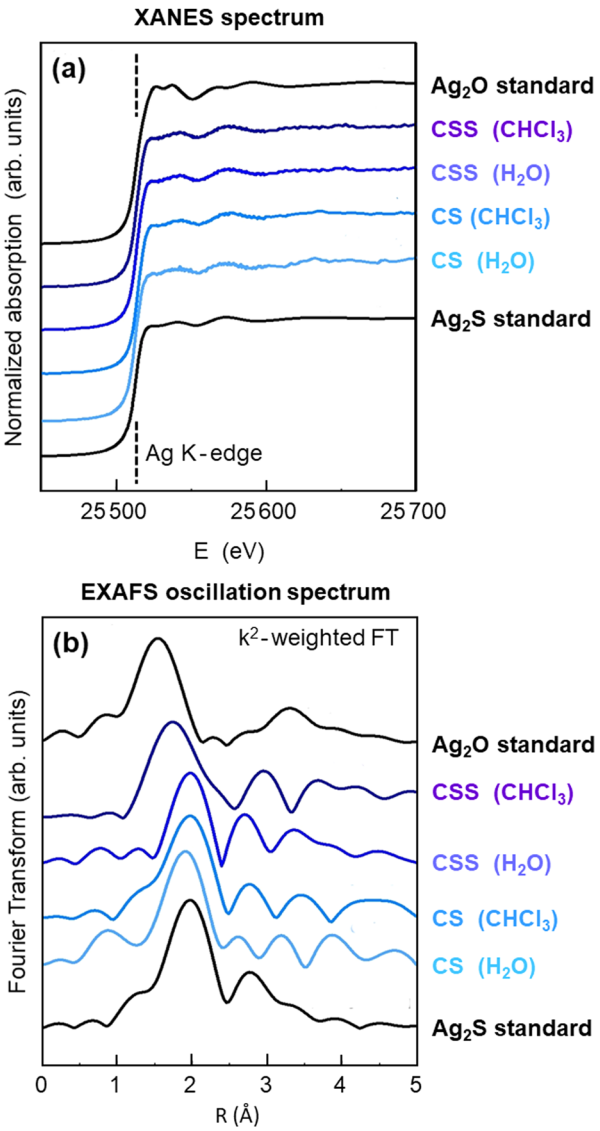

Fig. 4 (a) XANES spectra at the Ag K-edge of CS and CSS NCs solutions in $CHCl_3$ and water, compared with Ag_2S and Ag_2O standards. (b) Fourier transform (FT) of the k^2-weighted EXAFS oscillations, for all NCs systems shown in (a).

similar oxidation state of Ag in all them. However, clear differences can be observed in Fig. 4b, showing the k^2-weighted Fourier transform (FT) of the EXAFS oscillations for all systems.

The comparison of the FT maxima with those corresponding to Ag_2O and Ag_2S references (that account for the first Ag–O and Ag–S distances), evidences some signs of oxidation for the CSS samples in $CHCl_3$, compared to the sample transferred to water. Thus, these spectra indicate a better resistance to oxidation of the N-PMA samples (water) compared to those in $CHCl_3$. While the lower solubility of oxygen in water compared to that in $CHCl_3$ may partially explain this result, the better stability is mainly related to the more robust N-PMA shell for aqueous NCs compared to the oleylamine (OLA) surface ligands present on the Ag_2S NCs in $CHCl_3$ as will be evidenced further below.

Optical characterization with temperature and hyperspectral imaging

To evaluate the applicability of our step-wise systematically optimized NCs for NIR imaging and LNT, the temperature dependence of the PL properties of the CSS NCs produced in air was investigated. Fig. 5a and b show the temperature-dependent PL spectra of CSS in $CHCl_3$ and water, respectively. An increase in temperature induced a decrease in PL intensity and a redshift of the PL band, as previously reported for Ag_2S NPs produced by heat-up synthesis.[22] As the temperature increased, the emission intensity of the NCs decreased due to the activation of surface states that cause non-radiative luminescence quenching. Thermal vibrations increase ligand absorption/desorption rates, exposing more of the NC surface and creating defect states that can trap charge carriers, favouring non-radiative recombination and reducing the PL signal. Relative PLQY measurements using the fluorescent dye IR125 as a PLQY standard (PLQY of 13% in ethanol, see Methods in the eSI-S1, ESI†)[56] are displayed in Fig. 5c and d, yielding PLQY values of 9.2% and 2.7%, for the samples dispersed in $CHCl_3$ (Fig. 5c) and water (Fig. 5d), respectively. Note that these measurements were carried out six months after NCs synthesis. Although monoclinic Ag_2S and wurtzite ZnS crystalline lattices exhibit a large lattice mismatch,[26] the relatively high PLQY at RT of around 9–10%, exceeding reported values of around 4% for core/shell Ag_2S/ZnS.[31] suggests that with our strategy to add an intermediate synthesis step, including Se, and to perform the Zn treatment at relatively low temperature (60 °C) in air, we can nevertheless reduce the number of surface defects of the core without increasing the compression of its lattice.[26] The PLQY decrease in water is attributed to the labile ligands, mainly OLA, present on the NC surface.[21] OLA could hamper the complete intercalation of N-PMA between the alkyl moieties of OLA during the water transfer process.

Although Ag_2S NCs have been increasingly used as intensity-based luminescent thermometers, their temperature-dependence of PLQY has not been quantified before. In this work, the evolution of PLQY of CSS NCs in $CHCl_3$ and water with increasing temperature is shown in Fig. 5e. Also aging-induced PL changes have barely been assessed. The PLQY values of 9.2% and 2.7%

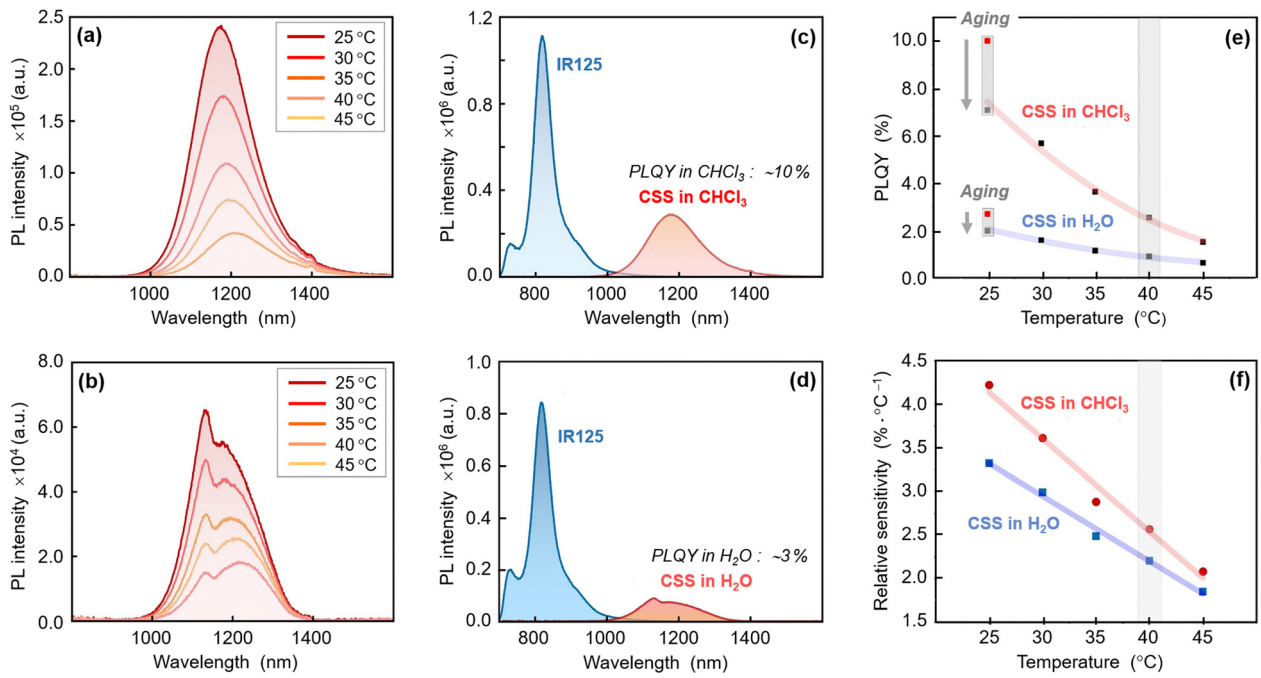

Fig. 5 PL response of CSS NCs to temperature in (a) chloroform and (b) water. Comparison of PL emission spectra with IR 125 dye (PLQY 13%) of CSS stored in (c) chloroform and (d) water. (e) PLQY dependence on temperature for CSS in chloroform and water. The labels "aging" denote a decrease in PLQY in two consecutive measurements carried out with 3 months of difference. Note that the first measurements were performed 6 months after synthesis. (f) Relative thermal sensitivity of CSS NCs in chloroform and water obtained 6 months after synthesis. The values of ΔS are three orders of magnitude smaller than those of S, and have been excluded from the plot.

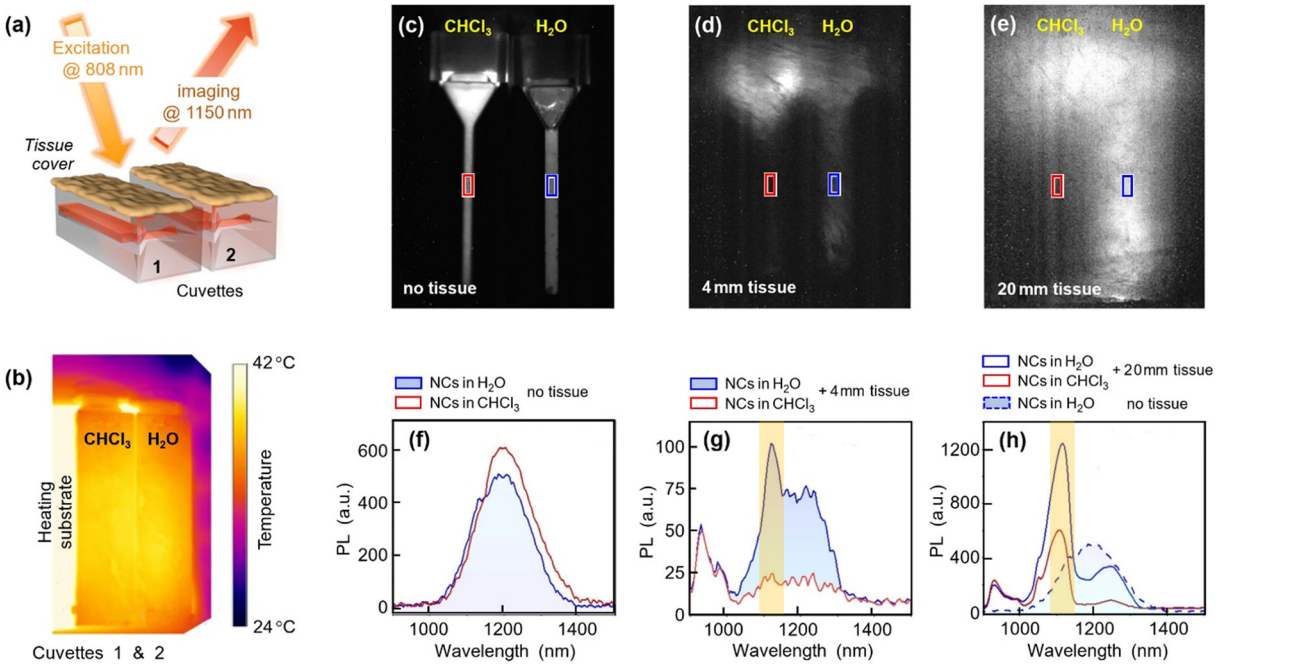

Fig. 6 (a) Sketch of the experiment where two cuvettes filled with NCs solution in chloroform (left) and water (right) were excited with an 808 nm laser and the NIR image was collected at 1150 nm. (b) The temperature of the solutions was measured using a thermal camera, pointing to ~40 °C under the tissue. (c)–(e) NIR images obtained without (c) or with 4 mm (d) and 20 mm (e) chicken breast tissue on top. The image shown in panel (c) was acquired with an integration time of 50 ms under a laser irradiance of 0.4 mW cm^{-2}. The data in panels (d) and (e) were acquired with an integration time of 100 ms and irradiance of 50 mW cm^{-2}, which is a very low value considering that the limit of *in vivo* experiments is set at 1 W cm^{-2}. (f) Comparative spectra of the NCs solution in chloroform (red) and water(blue) in the marked areas in panel (c). (g) Comparative spectra acquired from the marked areas when 4 mm tissue covers the cuvettes (red and blue for chloroform and water, respectively). The orange strip is related to the autofluorescence of the tissue. (h) Comparative spectra acquired from the marked areas when 20 mm tissue covers the cuvettes (red and blue for chloroform and water, respectively). The spectrum from the NCs solution in water is also included (dashed blue line). The orange strip is related to the autofluorescence of the tissue The control experiment, with water and without NCs (data not shown), showed no signal for this medium under these conditions.

measured 6 months after synthesis are indicated along with data measured after further 3 months. These measurements (labelled with the word "aging" in Fig. 5e) showed a slight decrease in PLQY from 9% to about 7% and from 2.7% to around 2.0% for the samples stored in $CHCl_3$ and water, respectively. These findings indicate a similar temporal influence (aging) on the PL intensity at RT (25 °C) in both samples, with a loss of at least 20% of the PL signal 9 months after synthesis. The evolution of PLQY with temperature shown in Fig. 5e revealed a more pronounced reduction for NCs in $CHCl_3$ than in water. As an example, the decrease is from 7% to 2% at 40 °C, while the PL in water only is reduced by 1% at the same temperature.

In order to evaluate and compare the NCs, temperature-dependent PL responses have been performed during three consecutive heating–cooling cycles (see Fig. S11 in eSI-2, ESI†). The results indicate partially irreversible PL quenching during the cycles mainly for CSS NCs in $CHCl_3$. In contrast, the temperature-dependent PL responses of CSS NCs in water remained constant across the three cycles, indicating that the NCs are significantly more robust against temperature changes.

As previously mentioned, the suitability for temperature sensing in LNT is compared, using their relative thermal sensitivity, S, as a figure of merit. S is calculated from the data summarized in Fig. 5a and b, and is presented in Fig. 5f (see Fig. S10 in eSI-S2 for calculations and details, ESI†). The S-values for samples stored in $CHCl_3$ and water, at approximately 40 °C, are close to 2.5 $°C^{-1}$ and 2.2% $°C^{-1}$, respectively. S is slightly higher for NCs in the former, in agreement with their reduced thermal stability compared to NCs in water. These S values are among the most competitive ones for Ag_2S NCs.[12,22]

To mimic *in vivo* conditions for NIR deep imaging and LNT applications, the performance of these CSS NCs at temperatures around 40 °C, under different tissue thicknesses, is illustrated in Fig. 6, modeling different penetrations depths. These experiments were performed to highlight the importance of known PLQY data at different temperatures for performance estimation and comparison. In this experiment, 350 μL of CSS NCs solutions in $CHCl_3$ (left) and water (right) matching optical densities were filled into two quartz cuvettes, that were then heated on a temperature controlled surface (see the sketch in Fig. 6a and a more detailed description in eSI-S1, ESI†) from RT to 40 °C for 3 h. A thermal imaging camera was used to control the temperature of the cuvettes under the chicken breast tissue (see Fig. 6b). Fig. 6c–e show the hyperspectral NIR images (acquired at 1150 nm) of the uncovered cuvettes (c) and covered with (d) 4- and (e) 20-mm thick chicken breast tissue, respectively (an optical image of the cuvettes with 20 mm chicken breast tissue on top can be seen in eSI-S1, ESI†). Fig. 6c shows that the emission of CSS NCs in $CHCl_3$ (left) is

significantly stronger than that in aqueous solution (right), according to the higher PLQY values shown in Fig. 5e. This is in good agreement with the hyperspectral PL response presented in Fig. 6f, corresponding to the marked areas (blue and red) in both cuvettes.

As expected, with the increasing thickness of the chicken breast tissue (Fig. 6d and e), the spatial resolution of the NIR images gradually decreased because of the strong attenuation and scattering of light by the tissue. In both cases, stronger signals were obtained for CSS NCs in water. Only this sample provides detectable PL signals at 40 °C. Thus, while higher initial PLQY values were observed for the samples in $CHCl_3$, a better NIR imaging of the entire cuvette section was observed for the NCs solution in water. In Fig. 6g the spectra extracted from the marked red and blue areas in Fig. 6d are compared: only the emission of the CSS NCs in water can be clearly detected. Fig. 6h provides a comparison between the spectra from the red and blue marked areas in Fig. 6e; this comparison reveals the absorption of chicken breast tissue and its impact on the PL band of the final spectrum. Similar distortions have been previously reported in the framework of LNT applications.[57,58]

The final PL line shape is the result of autofluorescence (marked with an orange strip) and intrinsic absorption of the components of the chicken breast tissue.[59] In the control experiment, with the cuvette filled with water and without NCs (data not shown), no signal was observed for this medium under these conditions. The results shown in Fig. 6 highlight the improved robustness of N-PMA-functionalized CSS NCs, which indicates that during the heating process, temperature-dependent PL quenching process occurred to a different extent in both solutions.

Our results highlight the crucial role of the surface passivating ligands. In the aqueous solution of CSS NCs, the presence of N-PMA leads to the formation of a compact ligand shell,[25] which is denser and more robust than the capping shell of NCs in $CHCl_3$ (mainly labile OLA ligands).[21] This accounts for the enhanced thermal stability of the CSS NCs passivated with N-PMA in water compared to CSS NCs in $CHCl_3$. Previous studies on Ag_2S core NCs produced by heat-up synthesis, exhibiting a relative thermal sensitivity higher than 4% $°C^{-1}$ at 38 °C, failed to allow for imaging deeper than 6 mm through similar tissues.[22] Furthermore, similar experiments showed the impossibility to work with the PL spectrum at locations deeper than 4–7 mm thick tissue.[12,60] The performance of the CSS NCs reported in this work suggests that these NCs might be superior candidates for NIR deep imaging and luminescence thermometry applications based on changes in the PL spectrum. The PL signal observed in the NIR images clearly correlates with the brightness of the NCs. As shown in Fig. S12 in eSI-2 (ESI†) the variation in absorption with temperature of the NCs solutions is negligible. Thus, the decrease in the PL signal in the NIR images is mainly caused by temperature-induced changes in PLQY. This underlines the importance of temperature-dependent PLQY studies for deep NIR imaging and LNT applications. These findings also underline the importance of utilizing temperature-dependent PLQY for optimizing materials for practical bioimaging, particularly for applications in LNT, where a high PL efficiency over a broad temperature range is desired.

Conclusion and outlook

This study presents a straightforward synthetic strategy for producing optimized Ag_2S-based nanocrystals (NCs) composed of Ag_2S cores and a gradated shell incorporating Se and Zn. The resulting NCs exhibit high photoluminescence quantum yield (PLQY), with values around 10% in chloroform and 3% after transfer to water using a biocompatible polymer. Notably, the highest PLQY values are achieved when the synthesis is conducted in air, which, according to XPS analysis, is attributed to increased Zn integration into the crystalline lattice. For the first time, we report on the temperature-dependent variations in PLQY for these NCs—a critical factor for imaging applications and a pioneering step in temperature studies for Ag_2S NCs. Our findings demonstrate that Ag_2S-based NCs with the highest PLQY in chloroform ($\sim$10%) are inefficient for imaging at 40 °C under 20 mm of tissue. In contrast, NCs in water with an initial PLQY of 2% provide superior tissue penetration and imaging clarity, emphasizing the importance of a robust ligand shell. Additionally, Ag_2S-based NCs with a PLQY of $\sim$2% in water at 40 °C, maintained for at least 3 hours, enable reasonable subcutaneous imaging under 20 mm of tissue using low laser power densities (up to 50 mW cm^{-2}) and short acquisition times (up to 100 ms), surpassing previous studies limited to a few millimeters. We believe these results will aid in the rational design of multifunctional NCs for NIR applications and set a new standard for comparing NCs in subcutaneous imaging and luminescence nanothermometry with NCs in the NIR range.

Author contributions

Peijiang Wang: investigation, visualization; Rafael Morales-Márquez: investigation; Gabriel Cervás: investigation; Alejandro Hernández Medel: investigation, visualization; Marina Paris Ogayar: investigation; D. Jimenez de Aberasturi: resources, writing – review & editing; Ana Ines de Isidro-Gomez: investigation; Almudena Torres-Pardo: investigation; visualization Francisco Javier Palomares: investigation; visualization Saül Garcia-Orrit: investigation; Celia Tavares: resources, funding acquisition; Ana Espinosa: funding acquisition, supervision; Helmut H. Telle: visualization, writing – review & editing; Dirk H. Ortgies: investigation, writing – review & editing; Víctor Vega-Mayoral: investigation, visualization, writing – original draft; Juan Cabanillas-González: writing – original draft; Emma Martín Rodríguez: investigation, funding acquisition, writing – review & editing; Ute Resch-Genger: writing – review & editing; K. David Wegner: investigation, writing – review & editing; Beatriz H. Juarez: conceptualization, methodology, visualization, funding acquisition, writing – original draft.

Data availability

All research data related to this article (including images and datasheets) will be published in the DIGITAL.CSIC repository at **https://digital.csic.es/?locale=en**.

Conflicts of interest

The authors declare no conflicts of interest.

Acknowledgements

This work was financed by the Spanish Ministerio de Ciencia, Innovación y Universidades/Agencia Estatal de Investigación (MICIU/AEI) through: PID2020-118878RB-I00 (RETINanoTHERMIA), 10.13039/501100011033, PID2023-151371OB-C21 and C-22 and PID2021-127033OB-C21, PID2019-106211RB-I00 (NANONERV) by MCIN/AEI/10.13039/501100011033, by the Instituto de Salud Carlos III (PI19/00565). D. H. O. is grateful for a "Ramón y Cajal" Contract RYC2022-036732-I funded by MCIN/AEI/10.13039/501100011033 and by "ESF investing in your future". M. O. thanks Ministerio de Universidades for her scholarship (FPU20/03166). R. M. M. thanks AEI for his grant PRE2022-104124, Severo Ochoa. F. J. P. acknowledges financial support from grant PID2021-126169OB-I00 funded by MCIN/AEI/10.13039/501100011033 and by "ERDF A way of making Europe". Additional funding was received by Comunidad de Madrid and Universidad Autónoma de Madrid (Project SI3/PJI/2021-00211), and by Grant Comunidad Autónoma de Madrid (CAM) S2022/BMD-7403 RENIM-CM grant, and co-financed by the European Structural and Investment Fund. V. V.-M. acknowledges grant TED2021-131906A-100 funded by Spanish Ministry of Science, Innovation and Universities (10.13039/501100011033) and financial support from the Regional Government of Madrid through grant 2019-T2/IND-12737. J. C.-G. acknowledge the MICINN-FEDER (PID2021-128313OB-I00), and support from the Regional Government of Madrid (NMAT2D-CM). J. C. G. also acknowledges a Research Consolidation Grant (CNS2022-36191) from the Spanish Ministry of Science and Innovation. IMDEA Nanociencia acknowledges support from the 'Severo Ochoa' Programme for Centres of Excellence in R&D of the Spanish Ministry of Science and Innovation (CEX2020-001039-S). S. G.-O. is grateful to the Spanish Ministry of Science and Innovation for a PhD grant (FPI, PRE2019-09345). C. T. S. acknowledges the program Atracción de Talento (CAM), ref. 2020-T1/IND-19889. We thank the BM30 beamline staff (ESRF synchrotron, Grenoble, France) for their support during the experiments. P. W. thanks CSS for his scholarship no. 202304910071.

References

1 E. Desurvire, *Erbium-Doped Fiber Amplifiers: Principles and Applications*, Wiley, Wiley-VCH Verlag GmbH & Co. KGaA, 2002.
2 Y. Liu, J. Li, J. Xiahou and Z. Liu, *J. Fluoresc.*, 2023, DOI: 10.1007/s10895-023-03513-8.
3 A. M. Smith, M. C. Mancini and S. Nie, *Nat. Nanotechnol.*, 2009, **4**, 710–711.
4 W. H. M. C. Amann, *Springer Handbook of Electronic and Photonic Materials*, Springer US, 2007.
5 D. Franke, D. K. Harris, O. Chen, O. T. Bruns, J. A. Carr, M. W. B. Wilson and M. G. Bawendi, *Nat. Commun.*, 2016, **7**, 12749.
6 F. Wang, Y. Zhong, O. Bruns, Y. Liang and H. Dai, *Nat. Photonics*, 2024, **18**, 535–547.
7 G. Hong, J. T. Robinson, Y. Zhang, S. Diao, A. L. Antaris, Q. Wang and H. Dai, *Angew. Chem., Int. Ed.*, 2012, **51**, 9818–9821.
8 J. Zhou, B. del Rosal, D. Jaque, S. Uchiyama and D. Jin, *Nat. Methods*, 2020, **17**, 967–980.
9 C. D. S. Brites, P. P. Lima, N. J. O. Silva, A. Millan, V. S. Amaral, F. Palacio and L. D. Carlos, *Nanoscale*, 2012, **4**, 4799–4829.
10 R. Piñol, J. Zeler, C. D. S. Brites, Y. Gu, P. Téllez, A. N. Carneiro Neto, T. E. da Silva, R. Moreno-Loshuertos, P. Fernandez-Silva, A. I. Gallego, L. Martinez-Lostao, A. Martínez, L. D. Carlos and A. Millán, *Nano Lett.*, 2020, **20**, 6466–6472.
11 B. del Rosal, D. Ruiz, I. Chaves-Coira, B. H. Juárez, L. Monge, G. Hong, N. Fernández and D. Jaque, *Adv. Funct. Mater.*, 2018, **28**, 1806088.
12 Y. Shen, J. Lifante, I. Zabala-Gutierrez, M. de la Fuente-Fernández, M. Granado, N. Fernández, J. Rubio-Retama, D. Jaque, R. Marin, E. Ximendes and A. Benayas, *Adv. Mater.*, 2022, **34**, 2107764.
13 F. Vetrone, R. Naccache, A. Zamarrón, A. Juarranz de la Fuente, F. Sanz-Rodríguez, L. Martinez Maestro, E. Martín Rodriguez, D. Jaque, J. García Solé and J. A. Capobianco, *ACS Nano*, 2010, **4**, 3254–3258.
14 S. K. Arumugasamy, G. Chellasamy, N. Murugan, S. Govindaraju, K. Yun and M.-J. Choi, *Adv. Colloid Interface Sci.*, 2024, **331**, 103245.
15 Z. Rao, Z. Li, X. Zhao and X. Gong, *Mater. Horiz.*, 2023, **10**, 1816–1824.
16 S. Otto, N. Scholz, T. Behnke, U. Resch-Genger and K. Heinze, *Chem. – Eur. J.*, 2017, **23**, 12131–12135.
17 Y. Shen, J. Lifante, E. Ximendes, H. D. A. Santos, D. Ruiz, B. H. Juárez, I. Zabala Gutiérrez, V. Torres Vera, J. Rubio Retama, E. Martín Rodríguez, D. H. Ortgies, D. Jaque, A. Benayas and B. del Rosal, *Nanoscale*, 2019, **11**, 19251–19264.
18 H. Shen, X. Jiao, D. Oron, J. Li and H. Lin, *J. Power Sources*, 2013, **240**, 8–13.
19 Y. Zhang, Y. Liu, C. Li, X. Chen and Q. Wang, *J. Phys. Chem. C*, 2014, **118**, 4918–4923.
20 Y. Zhang, G. Hong, Y. Zhang, G. Chen, F. Li, H. Dai and Q. Wang, *ACS Nano*, 2012, **6**, 3695–3702.
21 D. Ruiz, M. Mizrahi, H. D. A. Santos, D. Jaque, C. M. S. Jones, J. Marqués-Hueso, C. Jacinto, F. G. Requejo, A. Torres-Pardo, J. M. González-Calbet and B. H. Juárez, *Nanoscale*, 2019, **11**, 9194–9200.
22 D. Ruiz, B. del Rosal, M. Acebrón, C. Palencia, C. Sun, J. Cabanillas-González, M. López-Haro, A. B. Hungría, D. Jaque and B. H. Juarez, *Adv. Funct. Mater.*, 2017, **27**, 1604629.
23 A. Bera, S. S. Pathak, V. Kotha and B. L. V. Prasad, *Adv. Mater. Interfaces*, 2021, **8**, 2100898.
24 W. van der Stam, F. T. Rabouw, J. J. Geuchies, A. C. Berends, S. O. M. Hinterding, R. G. Geitenbeek, J. van der Lit,

S. Prévost, A. V. Petukhov and C. de Mello Donega, *Chem. Mater.*, 2016, **28**, 6381–6389.
25 A. Coro, A. Herrero Ruiz, M. Pazo-González, A. Sánchez-Cruz, T. Busch, A. Hernández Medel, E. C. Ximendes, D. H. Ortgies, R. López-Méndez, A. Espinosa, D. Jimenez de Aberasturi, D. Jaque, N. Fernández Monsalve, E. J. de la Rosa, C. Hernández-Sánchez, E. Martín Rodríguez and B. H. Juárez, *Small*, 2023, **19**, 2305026.
26 Y.-M. Zeng, L.-J. Pan, J. Wang, Y.-L. Fan, Y. Shu, D.-W. Pang and Z.-L. Zhang, *ChemistrySelect*, 2020, **5**, 5889–5894.
27 M. Karimipour, N. Moradi and M. Molaei, *J. Lumin.*, 2017, **182**, 91–97.
28 M. Karimipour, M. Bagheri and M. Molaei, *J. Electron. Mater.*, 2019, **48**, 2555–2562.
29 M. Karimipour, M. Bagheri and M. Molaei, *Mod. Phys. Lett. B*, 2017, **31**, 1750297.
30 Z. Tang, H. Yang, Z. Sun, Y. Zhang, G. Chen and Q. Wang, *Nano Res.*, 2023, **16**, 12315–12322.
31 P. Jiang, R. Wang and Z. Chen, *RSC Adv.*, 2015, **5**, 56789–56793.
32 L. Lv and H. Wang, *Mater. Lett.*, 2014, **121**, 105–108.
33 Y.-C. Pu, L.-C. Wang, S.-N. Wu, J.-C. Chang and C.-S. Yeh, *J. Phys. Chem. Lett.*, 2020, **11**, 2150–2157.
34 H. D. A. Santos, I. Zabala Gutiérrez, Y. Shen, J. Lifante, E. Ximendes, M. Laurenti, D. Méndez-González, S. Melle, O. G. Calderón, E. López Cabarcos, N. Fernández, I. Chaves-Coira, D. Lucena-Agell, L. Monge, M. D. Mackenzie, J. Marqués-Hueso, C. M. S. Jones, C. Jacinto, B. del Rosal, A. K. Kar, J. Rubio-Retama and D. Jaque, *Nat. Commun.*, 2020, **11**, 2933.
35 I. Z. Gutierrez, C. Gerke, Y. Shen, E. Ximendes, M. M. Silvan, R. Marin, D. Jaque, O. G. Calderón, S. Melle and J. Rubio-Retama, *ACS Appl. Mater. Interfaces*, 2022, **14**, 4871–4881.
36 J. W. de Wit, I. Zabala-Gutierrez, R. Marin, A. Zhakeyev, S. Melle, O. G. Calderon, J. Marques-Hueso, D. Jaque, J. Rubio-Retama and A. Meijerink, *J. Phys. Chem. Lett.*, 2024, **15**, 8420–8426.
37 T. Pellegrino, L. Manna, S. Kudera, T. Liedl, D. Koktysh, A. L. Rogach, S. Keller, J. Rädler, G. Natile and W. J. Parak, *Nano Lett.*, 2004, **4**, 703–707.
38 C. Renero-Lecuna, A. Herrero, D. Jimenez de Aberasturi, M. Martínez-Flórez, R. Valiente, M. Mychinko, S. Bals and L. M. Liz-Marzán, *J. Phys. Chem. C*, 2021, **125**, 19887–19896.
39 E. Peng, E. S. G. Choo, Y. Sheng and J. M. Xue, *New J. Chem.*, 2013, **37**, 2051.
40 W. Wang, A. Kapur, X. Ji, M. Safi, G. Palui, V. Palomo, P. E. Dawson and H. Mattoussi, *J. Am. Chem. Soc.*, 2015, **137**, 5438–5451.
41 M. G. Soliman, B. Pelaz, W. J. Parak and P. del Pino, *Chem. Mater.*, 2015, **27**, 990–997.
42 X. Zhuo, M. Henriksen-Lacey, D. Jimenez de Aberasturi, A. Sánchez-Iglesias and L. M. Liz-Marzán, *Chem. Mater.*, 2020, **32**, 5879–5889.
43 O. Veselska, C. Dessal, S. Melizi, N. Guillou, D. Podbevšek, G. Ledoux, E. Elkaim, A. Fateeva and A. Demessence, *Inorg. Chem.*, 2019, **58**, 99–105.
44 L. De Trizio and L. Manna, *Chem. Rev.*, 2016, **116**, 10852–10887.
45 B. Mao, C.-H. Chuang, F. Lu, L. Sang, J. Zhu and C. Burda, *J. Phys. Chem. C*, 2013, **117**, 648–656.
46 C. de M. Donegá, *Chem. Soc. Rev.*, 2011, **40**, 1512–1546.
47 M. Acebrón, J. F. Galisteo-López, D. Granados, J. López-Ogalla, J. M. Gallego, R. Otero, C. López and B. H. Juárez, *ACS Appl. Mater. Interfaces*, 2015, **7**, 6935–6945.
48 X. Zhang, J. Liu and E. M. J. Johansson, *Nanoscale*, 2015, **7**, 1454–1462.
49 J. Sun, W. Yu, A. Usman, T. T. Isimjan, S. DGobbo, E. Alarousu, K. Takanabe and O. F. Mohammed, *J. Phys. Chem. Lett.*, 2014, **5**, 659–665.
50 S. Lin, Y. Feng, X. Wen, T. Harada, T. W. Kee, S. Huang, S. Shrestha and G. Conibeer, *J. Phys. Chem. C*, 2016, **120**, 10199–10205.
51 T. Borzda, C. Gadermaier, N. Vujicic, P. Topolovsek, M. Borovsak, T. Mertelj, D. Viola, C. Manzoni, E. A. A. Pogna, D. Brida, M. R. Antognazza, F. Scotognella, G. Lanzani, G. Cerullo and D. Mihailovic, *Adv. Funct. Mater.*, 2015, **25**, 3351–3358.
52 E. A. A. Pogna, M. Marsili, D. De Fazio, S. Dal Conte, C. Manzoni, D. Sangalli, D. Yoon, A. Lombardo, A. C. Ferrari, A. Marini, G. Cerullo and D. Prezzi, *ACS Nano*, 2016, **10**, 1182–1188.
53 Q.-C. Sun, L. Yadgarov, R. Rosentsveig, G. Seifert, R. Tenne and J. L. Musfeldt, *ACS Nano*, 2013, **7**, 3506–3511.
54 J. Cabanillas-Gonzalez, T. Virgili, A. Gambetta, G. Lanzani, T. D. Anthopoulos and D. M. de Leeuw, *Phys. Rev. Lett.*, 2006, **96**, 106601.
55 V. Vega-Mayoral, T. Borzda, D. Vella, M. Prijatelj, E. A. A. Pogna, C. Backes, J. N. Coleman, G. Cerullo, D. Mihailovic and C. Gadermaier, *2D Mater.*, 2017, **5**, 015011.
56 J. Pauli, A. Güttler, T. Schneider, C. Würth and U. Resch-Genger, *Anal. Chem.*, 2023, **95**, 5671–5677.
57 J. Lifante, Y. Shen, I. Zabala Gutierrez, I. Rubia-Rodríguez, D. Ortega, N. Fernandez, S. Melle, M. Granado, J. Rubio-Retama, D. Jaque and E. Ximendes, *Adv. Sci.*, 2021, **8**, 2003838.
58 Y. Shen, J. Lifante, N. Fernández, D. Jaque and E. Ximendes, *ACS Nano*, 2020, **14**, 4122–4133.
59 J. Lifante, Y. Shen, E. Ximendes, E. Martín Rodríguez and D. H. Ortgies, *J. Appl. Phys.*, 2020, **128**, 171101.
60 H. Li, Z. Du, L. Zhu, C. Zhang, J. Xiong, B. Zhou, B. Dong, X. Zhang and N. Alifu, *ACS Appl. Mater. Interfaces*, 2024, **16**, 32045–32057.

